JOURNAL OF MATERIALS SCIENCE 31 (1996) 1455–1468

# Microstructural and mechanical characterization of laser-beam welding of a 8090 Al–Li thin sheet

M. F. LEE, J. C. HUANG, N. J. HO
*Institute of Materials Science and Engineering, National Sun Yat-Sen University, Kaohsiung, Taiwan*

In extension to a previous study on electron-beam welding (EBW) under vacuum on a 8090 thin sheet, the current paper reports the parallel results of laser-beam welding (LBW) of the same material. Autogenous "bead-on-plate" laser-beam welding was performed by a 3 kW $CO_2$ LBW machine. The power of the input laser beam, the specimen moving speed, and the focusing condition was varied from 700 to 1300 W, 1500 to 9000 mm $min^{-1}$, and 1 to 3 mm below the specimen top surface, respectively. The protection atmosphere and plasma jet were achieved by blowing either Ar or $N_2$ gas. The effects of using different gases were evaluated in terms of weld-line appearance, fusion-zone dimension, solute evaporation, microhardness, post-weld tensile properties, as well as porosity distribution. In comparing with the EBW results, LBW on the 8090 alloy was characterized with a higher fusion-zone depth/width ratio, cooling rate and porosity amount, and a lower solute loss and post-weld tensile strain. The primary formation mechanism for porosity was thought to be related to the collapsed key-holes during LBW under Ar or $N_2$ and the hydride-induced gas pores during EBW under vacuum.

## 1. Introduction

Al–Li alloys have been discovered to possess supreme superplasticity under appropriate conditions [1]. In order to apply the gas blowing superplastic forming (SPF) technique to fabricate sophisticated aircraft components, a bonding technique has to be coupled with SPF routines. Diffusion bonding, which has been successfully applied for superplastic Ti alloys, was the first choice in Al research circles [2–5]. However, the stable surface oxide layer on Al alloys presents problems during SPF/diffusion bonding practices, except under vacuum. A previous study [6] on electron beam welding (EBW) of superplastic 8090 Al–Li thin sheets has demonstrated the characteristics and feasibility of EBW/SPF combinations. The current paper reports the fundamental microstructural and mechanical characterization of autogenous "bead-on-plate" laser beam welding (LBW) on this material. Emphasis will be put on the effects of blowing different gases and the distribution of porosity. Results on more application-orientated aspects, such as systematic shear lap and peel tests and LBW/SPF combinations will be presented elsewhere.

The welding characteristics of the Al–Li base alloys have been studied by a number of investigators, e.g. Refs. 7–20. However, very few reports were concentrated on laser welding of this material. In considering the LBW performance in Al base alloys, there are several factors needed to be considered, namely, (1) the high thermal conductivity, (2) high thermal expansion, (3) high chemical reactivity, (4) high reflectivity against laser beam, (5) high fluidity, (6) high vapour pressure, (7) low melting temperature, and (8) low ionization energy. The presence of Li and Mg in the 8090 Al–Li base alloy will further worsen some of the behaviours, e.g. factors (3), (6) and (8), but improves somewhat in factor (1).

In general, the absorption efficiency for $CO_2$ laser with 10.6 μm wavelength by most metallic materials was quite low, for example, the absorption portion by Al was only 2% at room temperature and less than 4% at 1000 °C [21]. However, once the input laser power density reaches a critical value ($\sim 10^4$ W $mm^{-2}$ for metals), plasma will be induced and the workpiece absorption rate rises significantly [22]. At even higher power input, a lower absorption will again result due to the strong plasma shielding. Aluminium alloys are characterized by their low ionization energy, resulting in a high tendency to form a plasma plume above the workpiece. This effect will be beneficial to the initial stage, but detrimental to later stages (once a stable key-hole is established) due to the plasma screening effect.

The high thermal conductivity will generally widen the weld line considerably if the welding speed is not high enough. Cross *et al.* [9] have found that the weld penetration during arc welding will increase with increasing Li content due to the fact that Li can reduce thermal conductivity (by ~ 30% versus other Al alloys) making the input heat concentrated and promoting deeper penetration. The lower thermal conductivity has also been claimed to be beneficial to laser beam welding by the same reason [11]. On the other hand, the high thermal expansion coefficient of Al

0022–2461  

alloys also lead to high residual stress and a high number of dislocations upon cooling from the weld temperature. When coupled with the strong solute segregation, or when local precipitation near grain boundary regions occurred during solidification, specimen distortion or even hot cracking might be induced. For Al–Li base alloys, the hot cracking susceptibility was found to increase with increasing Li content up to 2.6 wt % followed by a gradual decrease [9]. This problem may be avoided by decreasing the heat input or increasing the welding speed [6].

Owing to the high fluidity and high vapour pressure of Al alloys, the key-hole during welding is less stable compared with those in steels, resulting in the tendency to form pores, splashes, fluctuation of weld depth, and unevenness of the weld top-surface. Generally, gas pores were found to be present in most cases [7, 10, 13, 14].

## 2. Experimental methods

The material used was the commercial superplastic 8090 Al sheet of 1.6 mm in thickness (hereafter referred as SPF-8090). The chemical composition was Al–2.40%Li–1.30%Cu–0.63%Mg–0.11%Zr (in weight percent), plus minor Ti, Si, Fe, and Zn (all $\leq 0.05\%$). This SPF-grade sheet has been subjected to a series of thermomechanical treatments in order to achieve satisfactory superplastic properties, and possessed unrecrystallized fine equiaxed subgrains of size $\sim 4.5\ \mu m$. The as-received material was observed to contain fine $\delta'$ ($Al_3Li$) precipitates 3 nm in diameter and $\beta'$ ($Al_3Zr$) dispersoids 30–40 nm in size.

The surface treatment in this study included mechanical grinding to remove the surface layer by 30–40 μm, followed by ultrasonic cleaning in acetone. To reduce surface reflection against the laser beam, a final grinding before acetone cleaning was done using a #60 coarse emery paper. Autogenous "bead-on-plate" laser beam welding was performed by the PRC 3 kW $CO_2$ LBW machine with a 127 mm focal lense. Below the workpiece, Cu blocks were placed to enhance heat transfer. The protection atmosphere was maintained by blowing either Ar or $N_2$ gas to the top and bottom sides of the welded specimen, the gas flow rate was $40\ l\ min^{-1}$ for the top side and $2.5\ l\ min^{-1}$ for the bottom side. A plasma-jet which was used to reduce the induced plasma plume was achieved also by blowing either Ar or $N_2$ gas through a jet outlet, with a 0.7 mm inner diameter, positioned 2.5 mm above and 4.5 mm apart from the weld pool. The gas flow rate of the plasma-jet was $1\ l\ min^{-1}$ and the blowing direction was the same as the specimen moving direction. The current gas flow rates used were selected after numerous trials, and were considered to be within the optimum range. Influence from varying gas flow rates was not included in the present study. It should be noted that when one gas type was selected all three gas outlets would release the same type of gas, thus the effects of using different gases can be evaluated in terms of weld line appearance, fusion zone dimension, post-weld tensile property, as well as porosity distribution. For simplicity, hereafter the specimens welded using Ar or $N_2$ gas will be termed as the Ar or $N_2$ specimens, respectively.

The power of the input laser beam, the specimen moving speed, and the focusing condition were varied from 700 to 1300 W, 1500 to 9000 mm $min^{-1}$, and +1 to +3 mm (+ meaning below the specimen top surface), respectively, as tabulated in Tables I and II for the cases using Ar and $N_2$. The above LBW parameters were also chosen as within the optimum range after preliminary trials. Although a lower weld speed, coupled with a higher power, might help to reduce the pore amount in the fusion zone, such combinations were found to be unsatisfactory since the weld line would widen significantly. For all the LBW experiments, the weld line was perpendicular to the original rolling direction of the superplastic sheets. The specimen was placed in the welding machine with double clips. The working distance was 900 mm and the beam was focused below the top surface with a beam size around 0.1 mm, corresponding to a power density in the neighborhood of $10^5\ W\ mm^{-2}$. Due to strong absorption of the incoming laser beam by the plasma, the actual values of power density and heat input to the specimen cannot be evaluated.

The as-received and the as-welded specimens were subjected to the standard T6 treatment, which comprised solution treatment at 530 °C for 2 h in a salt bath followed by water quenching and ageing at 170 °C for 32 h in an oil bath. Microhardness measurements were conducted on selected specimens using an Akashi Vickers machine, with a load of 25 g and duration of 15 s. Tensile tests were performed using the Instron 1125 system at a strain rate of $10^{-3}\ s^{-1}$. The loading direction was perpendicular to the weld line, and thus parallel to the original rolling direction of the sheet. The tensile specimens were of 10 mm gauge length and 3 mm width. Before tensile tests, the post-weld specimens were mechanically ground to remove the surface unevenness and undercut, as well as the bottom unpenetrated part for those specimens that were not fully penetrated by the laser beam.

TABLE I The weld parameters used for the Ar specimens

| No. | Power (W) | Speed (mm $min^{-1}$) | Heat input (kJ $m^{-1}$) | Focus (mm) |
|---|---|---|---|---|
| 501 | 700 | 1500 | 28.0 | +1 |
| 502 | 700 | 2000 | 21.0 | +1 |
| 503 | 700 | 2000 | 21.0 | +2 |
| 504 | 700 | 2200 | 19.1 | +2 |
| 505 | 700 | 2500 | 16.8 | +1 |
| 506 | 700 | 2500 | 16.8 | +1.5 |
| 507 | 900 | 3000 | 18.0 | +2 |
| 508 | 900 | 3500 | 15.4 | +2 |
| 509 | 900 | 4000 | 13.5 | +1 |
| 510 | 900 | 4000 | 13.5 | +2 |
| 511 | 1100 | 5000 | 13.2 | +2 |
| 512 | 1100 | 5500 | 12.0 | +2 |
| 513 | 1100 | 6500 | 10.1 | +2 |
| 514 | 1100 | 7500 | 8.8 | +1 |
| 515 | 1100 | 7500 | 8.8 | +2 |
| 516 | 1300 | 6000 | 13.0 | +2 |
| 517 | 1300 | 7000 | 11.1 | +2 |
| 518 | 1300 | 7500 | 10.4 | +2 |
| 519 | 1300 | 9000 | 8.7 | +2 |

TABLE II The weld parameters used for the $N_2$ specimens

| No. | Power (W) | Speed ($mm\,min^{-1}$) | Heat input ($kJ\,m^{-1}$) | Focus (mm) |
|---|---|---|---|---|
| 601 | 900 | 2500 | 21.60 | +1 |
| 602 | 900 | 2500 | 21.60 | +2 |
| 603 | 900 | 3000 | 18.00 | +1 |
| 604 | 900 | 3000 | 18.00 | +2 |
| 605 | 900 | 3000 | 18.00 | +2.5 |
| 606 | 900 | 3000 | 18.00 | +3 |
| 607 | 900 | 3500 | 15.43 | +1 |
| 608 | 900 | 3500 | 15.43 | +2 |
| 609 | 900 | 4000 | 13.50 | +2 |
| 610 | 1100 | 4500 | 14.67 | +2 |
| 611 | 1100 | 4500 | 14.67 | +2.5 |
| 612 | 1100 | 5000 | 13.20 | +2 |
| 613 | 1100 | 5000 | 13.20 | +2.5 |
| 614 | 1100 | 5500 | 12.00 | +2 |
| 615 | 1100 | 6000 | 11.00 | +2 |
| 616 | 1100 | 7000 | 9.43 | +2 |

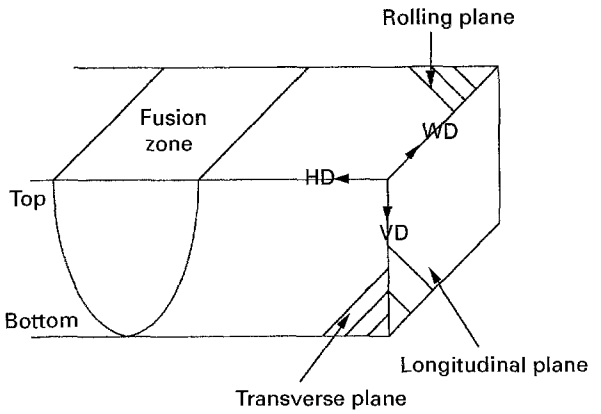


*Figure 1* Schematic illustration of the related planes and directions in the weld specimens. HD, VD, and WD refer to the horizontal, vertical, and welding direction, respectively. The horizontal direction is the same as the rolling direction.

The solute segregation effect was characterized by electron probe microanalysis (EPMA) using the Cameca-SX50 system. The microstructure and fracture surface were characterized by optical microscopy (OM) as well as scanning electron microscopy (SEM). The porosity distribution inside the fusion zone was revealed by radiography and SEM. To measure the pore area fraction in the interior of the fusion zone, the as-welded specimen was ground along the horizontal or vertical direction, respectively (cf. Fig. 1), taking OM or SEM photos for each longitudinal or rolling plane after 0.1–0.15 mm material removal. Thus the pore size and porosity area-fraction variation, measured on the longitudinal and rolling planes, can be individually established.

## 3. Results

### 3.1. Macro-appearance revealed by optical microscopy

The typical top-view appearances of the weld line when LBWed under Ar and $N_2$ are shown in Fig. 2. For the Ar specimens the weld lines were seen to change from a smooth surface at low power and low welding speed, to ripple appearance at intermediate power and welding speed (Fig. 2(a)), and to irregular surface at high power and high welding speed. The weld lines welded under $N_2$ appeared to be less smooth and less shiny, possessing sand-like fine particles which are most likely products of nitride (Fig. 2(b)). The typical fusion zones seen from the transverse plane are shown in Fig. 2(c) and (d) for the Ar specimens welded at low and high power. The humping effect [23, 24] (a central hump together with two undercuts on both sides, as in Fig. 2(d) was frequently observed in samples with deep fusion zones, suggesting the inward and downward flowing trend of the melt. Undercut (Fig. 2(d)) at the top surface was observed in samples welded under both Ar and $N_2$ atmosphere at high powers and high welding speeds, but the problem was more severe in the $N_2$ specimens, which might be due to the difference in surface tension and melt flowing direction under these two situations (Section 4.1). Meanwhile, the weld surface in samples using "focus +2" appeared to be more uneven than that when using "focus +1". This might be due to the better heat absorption efficiency in the former cases, leading a deeper key-hole and more violent stir inside the fusion zone.

### 3.2. Cross-sectional area of fusion zone

Since the actual heat absorption during LBW was much lower than the heat input, an indication closely related to the heat absorption, such as the cross-sectional area of the FZ (termed as $A_f$), becomes an important index. Tables III and IV and Fig. 3 present the dependence of $A_f$ as a function of heat input under Ar or $N_2$. A positive trend was basically followed, except when welded at high powers (1100 or 1300 W) where a discontinuous jerk was seen. The latter was caused by the plasma-screening effect, which was most serious for the nearly penetrated welds (point A in Fig. 3) and became suddenly released from the bottom surface upon full penetration (point B). Comparing the cases under Ar and $N_2$, the cross-sectional area in the latter case was smaller by $\sim 40\%$. This was primarily caused by the narrower fusion zone under the $N_2$ atmosphere.

Focusing condition also imposed a direct influence on the cross-sectional area. Under the same power and welding speed, the dependence of $A_f$ with respect to the focusing condition showed a descending trend according to the order "focus +2" $>$ +1.5 $>$ +1 $>$ +2.5 $>$ +3. Taking "focus +2" as a reference, the lower $A_f$ values for focusing above this point (e.g. +1.5) should be due to the accelerated plasma screening and that for focusing below should be owing to the lower power density.

### 3.3. Depth to width ratio

The data on depth ($D$), width ($W$, measured from the top surface), and their ratio ($D/W$) of the fusion zone are also included in Tables III and IV and the relationship between $D/W$ and heat input for the Ar and $N_2$ cases is shown in Fig. 4. The top-surface width of

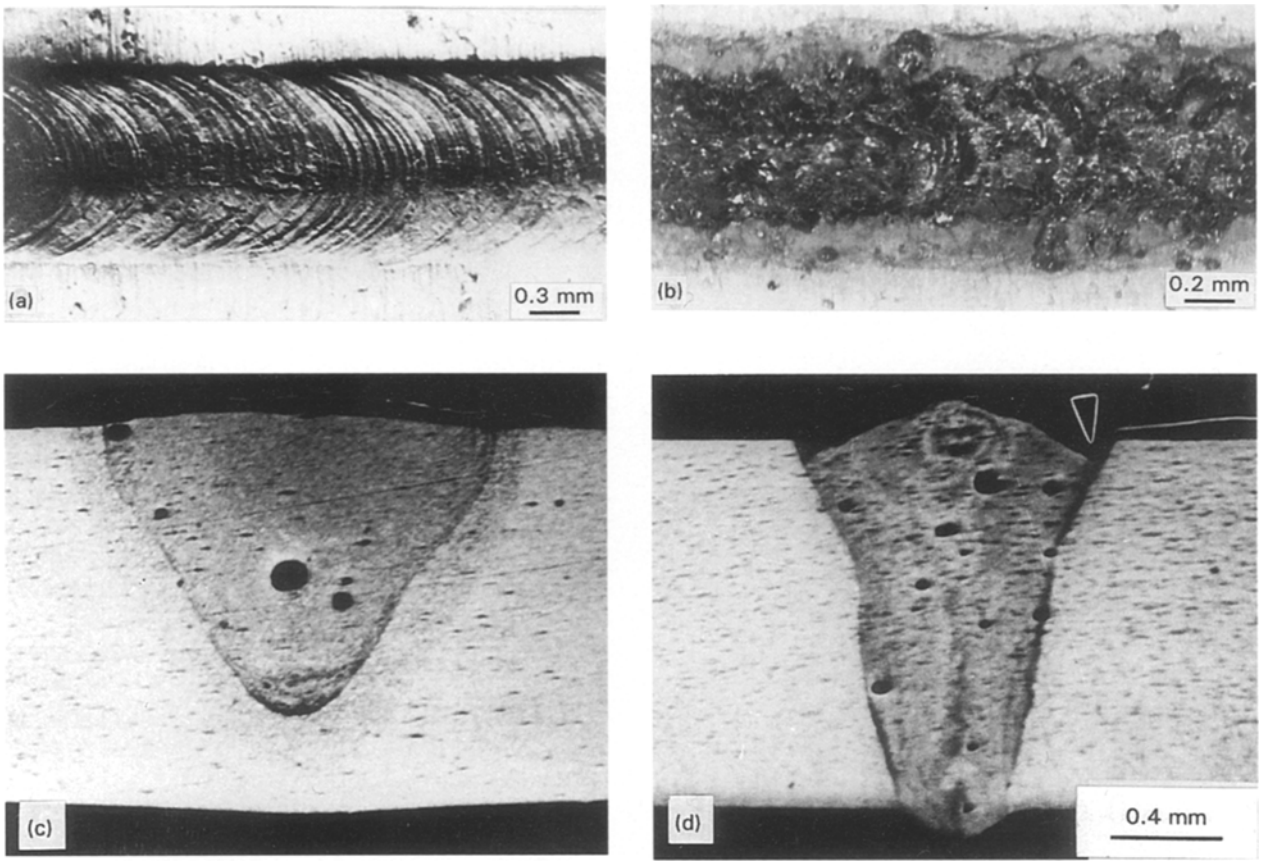


*Figure 2* Typical optical micrographs of the fusion zones seen from the top surface: (a) the Ar specimen 505, and (b) the $N_2$ specimen 601; or from the transverse surface: (c) the Ar specimen 502, and (d) the Ar specimen 518.

TABLE III Summary of the microstructural characteristics seen in the Ar specimens. $A_f$, $D$ and $W$ are the cross-sectional area, depth, and top-surface width, respectively, of the fusion zone. $P_{l,max}$ and $P_{r,max}$ are the maximum porosity area fractions measured from the longitudinal and rolling plane, respectively

| No. | $A_f$ ($mm^2$) | $D$ (mm) | $W$ (mm) | $D/W$ ratio | $P_{l,max}$ (%) | $P_{r,max}$ (%) | $P_{l,max}/P_{r,max}$ |
|---|---|---|---|---|---|---|---|
| 501 | 2.04 | 1.58[a] | 1.98 | 0.79 | 5.5 | 7.2 | 0.75 |
| 502 | 1.02 | 1.20 | 1.63 | 0.75 | 10.4 | 5.1 | 2.04 |
| 503 | 1.64 | 1.58[a] | 1.61 | 0.98 | 12.7 | 6.4 | 1.96 |
| 504 | 1.01 | 1.28 | 1.53 | 0.84 | 9.0 | 5.2 | 1.73 |
| 505 | 0.68 | 1.03 | 1.28 | 0.80 | 4.7 | 1.6 | 2.90 |
| 506 | 1.06 | 1.36 | 1.52 | 0.90 | 9.4 | 6.1 | 1.54 |
| 507 | 1.67 | 1.58[a] | 1.60 | 0.99 | 14.8 | 6.6 | 2.24 |
| 508 | 1.61 | 1.58[a] | 1.46 | 1.08 | 19.2 | 10.7 | 1.79 |
| 509 | 0.73 | 1.12 | 1.27 | 0.88 | 3.2 | 2.9 | 1.09 |
| 510 | 0.96 | 1.41 | 1.33 | 1.06 | 6.6 | 6.4 | 1.03 |
| 511 | 0.94 | 1.42 | 1.30 | 1.09 | 12.7 | 8.0 | 1.59 |
| 512 | 1.12 | 1.58[a] | 1.20 | 1.32 | 5.7 | 8.3 | 0.68 |
| 513 | 0.96 | 1.21 | 1.55 | 0.78 | – | – | – |
| 514 | 0.60 | 1.05 | 1.11 | 0.94 | 2.9 | 6.3 | 0.47 |
| 515 | 0.79 | 1.29 | 1.18 | 1.09 | 8.0 | 4.7 | 1.70 |
| 516 | 1.59 | 1.58[a] | 1.29 | 1.22 | 3.1 | 7.0 | 0.44 |
| 517 | 1.31 | 1.58[a] | 1.19 | 1.33 | 7.4 | 5.6 | 1.33 |
| 518 | 1.46 | 1.58[a] | 1.32 | 1.20 | 9.9 | 4.7 | 2.13 |
| 519 | 0.77 | 1.29 | 1.17 | 1.11 | 14.0 | 5.4 | 2.59 |

[a] Means that a fully penetrated weld has been achieved.

TABLE IV Summary of the microstructural characteristics seen in the $N_2$ specimens

| No. | $A_f$ ($mm^2$) | $D$ (mm) | $W$ (mm) | $D/W$ ratio | $P_{l,max}$ (%) | $P_{r,max}$ (%) | $P_{l,max}/P_{r,max}$ |
|---|---|---|---|---|---|---|---|
| 601 | 1.30 | 1.58[a] | 1.09 | 1.45 | 4.7 | 3.2 | 1.47 |
| 602 | 1.44 | 1.58[a] | 1.17 | 1.35 | 4.8 | 4.1 | 1.17 |
| 603 | 0.80 | 1.51 | 1.07 | 1.41 | 5.6 | 2.2 | 2.55 |
| 604 | 1.04 | 1.58[a] | 1.07 | 1.48 | 6.4 | 3.1 | 2.06 |
| 605 | 0.67 | 1.35 | 1.00 | 1.35 | 5.8 | 3.3 | 1.75 |
| 606 | 0.62 | 1.16 | 1.07 | 1.09 | 2.6 | 2.4 | 1.08 |
| 607 | 0.66 | 1.35 | 0.98 | 1.38 | 5.0 | 1.7 | 2.94 |
| 608 | 0.75 | 1.44 | 1.05 | 1.38 | 6.3 | 3.6 | 1.75 |
| 609 | 0.56 | 1.18 | 0.94 | 1.26 | 5.4 | 3.8 | 1.42 |
| 610 | 1.28 | 1.58[a] | 1.07 | 1.48 | 5.0 | 4.8 | 1.04 |
| 611 | 0.72 | 1.38 | 1.05 | 1.32 | 8.7 | 5.3 | 1.64 |
| 612 | 1.19 | 1.58[a] | 1.02 | 1.55 | 6.8 | 2.1 | 3.24 |
| 613 | 0.59 | 1.28 | 0.93 | 1.38 | 4.7 | 3.4 | 1.38 |
| 614 | 0.64 | 1.37 | 0.93 | 1.48 | 11.0 | 2.0 | 5.50 |
| 615 | 0.67 | 1.42 | 0.95 | 1.49 | 6.3 | 2.0 | 3.15 |
| 616 | 0.52 | 1.16 | 0.89 | 1.30 | 4.7 | 3.4 | 1.38 |

[a] Means that a fully penetrated weld has been achieved.

the FZ when welded using Ar was mostly varied within 1.1 to 1.6 mm, compared with the narrower width when using $N_2$ (0.9–1.1 mm). Both ranges are considered to be rather narrow in comparison with our previous EBW results [6] or conventional welding [10]. The dependence of $D/W$ as a function of heat input can also be explained by the same argument applied to $A_f$, though the positive trend of $D/W$ became saturated once the weld was fully penetrated. In general, the narrowest FZ was achieved at the highest beam power coupled with the highest welding speed. Under the same power and welding speed, focus +2 generally yielded the deepest FZ, but exceptions were also occasionally observed.

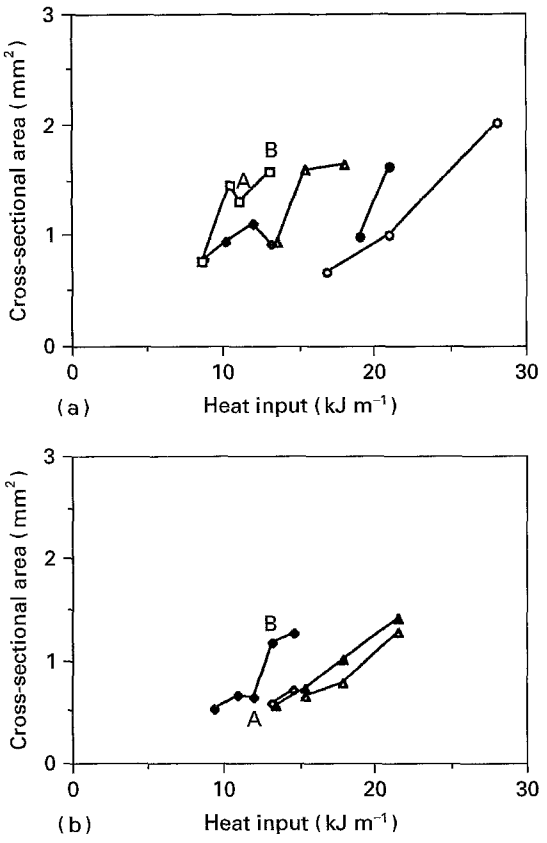


*Figure 3* Illustration of the dependence of fusion-zone cross-sectional area as a function of heat input for (a) the Ar specimens (○ 700 W/ + 1; ●700 W/ + 2; △ 900 W/ + 2; ◆ 1100 W/ + 2; □ 1300 W/ + 2), and (b) the $N_2$ specimens (△ 900 W/ + 1; ▲ 900 W/ + 2; ◆ 1100 W/ + 2; ◇ 1100 W/ + 2.5). Points A and B are referred to the nearly penetrated and fully penetrated fusion zone, respectively.

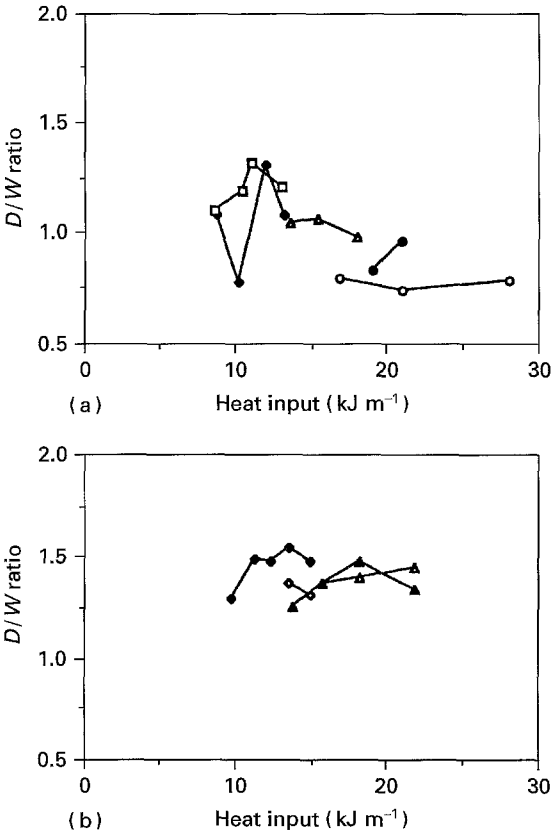


*Figure 4* Illustration of the dependence of fusion-zone depth/width ($D/W$) ratio as a function of heat input for (a) the Ar specimens, and (b) the $N_2$ specimens. See Fig. 3 for key.

## 3.4. Metallography

A typical metallographic micrograph from the transverse section of samples welded under Ar is shown in Fig. 5(a). The heat-affected zone, depending on the level of heat input, were ranged from 80 to 170 μm in width. Three regions, each with characteristic grains, were seen inside the fusion zone. Fine equiaxed grains measuring 3–6 μm were present along the fusion line (or chilled zone) due to rapid cooling. Next to the fusion line and extending inward for ~ 100–200 μm were there the columnar grains with a long axis 50–100 μm and a short axis 5–10 μm in length. At the centre of the fusion zone nearly equiaxed larger grains measuring 8–60 μm were observed. There appeared two kinds of grain groups within this central region (Fig. 5(b)). One exhibited brighter contrast after chemical etching with smaller grain sizes to 8–30 μm, possessing fewer precipitates of the S ($Al_2CuMg$) $T_1$ ($Al_2CuLi$) and $T_2$ ($Al_6Li_3Cu$) phases, and the other showed darker contrast with larger grain sizes to 20–60 μm, containing much more second phases. These brighter grain groups formed a river- or tree-branch pattern and were a result of different cooling history. The heat dissipation and temperature distribution should have been considerably non-uniform. For all of the three regions, the grain boundaries after chemical etching were well exposed and were seen to possess finite width. Based on the previous transmission electron microscopy study [6], the grain boundaries might be full of coarse second phases.

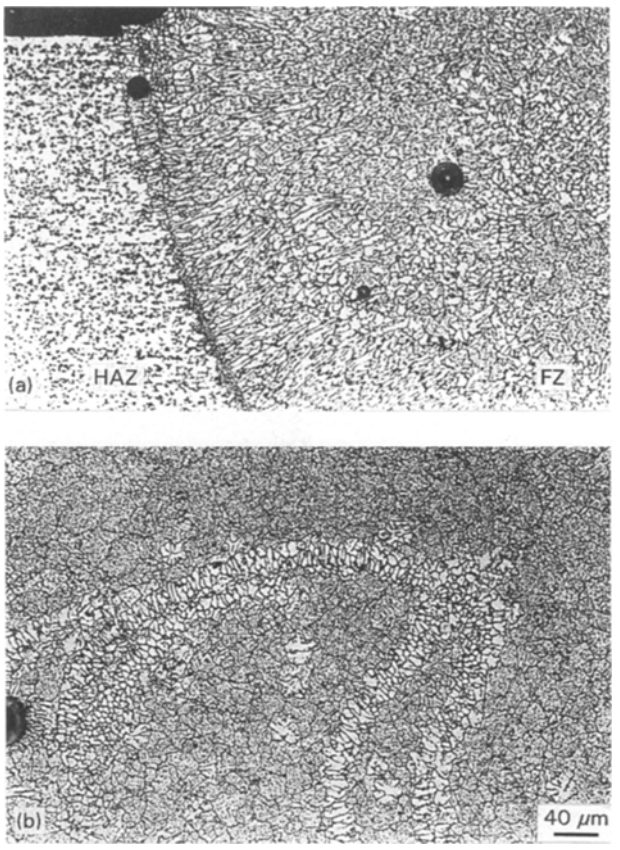


*Figure 5* Typical optical micrographs of (a) the grain structure seen from the transverse plane in the Ar specimen 507, and (b) the two kinds of grain group observed in the central region of a fusion zone in the Ar specimen 501. HAZ, heat-affected zone; FZ, fusion zone.

Due to faster heat transfer under $N_2$, the heat-affected zone width was smaller, ranging from 60 to 130 μm. Sometimes, only two regions were observed in the fusion zone, as there was almost no columnar region. For those very limited columnar grains, the length of the long axis was at most 20 μm, coupled with a length ~ 5 μm in the short axis. In general, the fine equiaxed chilled grains 2–5 μm in size along the fusion line were neighboured to the central nearly equiaxed grains measuring 6–15 μm. There were no or very few precipitates in the grain interior, again suggesting the faster cooling rate under $N_2$.

Since the welded piece will be usually subjected to a T6 temper following LBW, the microstructure after the solution treatment (530 °C for 2 h) was also examined. Examples are shown in Fig. 6. The grains inside the fusion zone, as well as some of gains in the heat-affected zone, grew significantly to even 200 μm. On the contrary, the grains in the base metal, which were away from the fusion and heat-affected zones and were more stable by the uniformly dispersed $Al_3Zr$ particles, grew slightly to ~ 8–10 μm, as typically seen for such superplastic thin sheets subjected to superplastic tension loading or forming at 510–530 °C for 1–2 h [25]. It seemed that the recrystallized grains inside the fusion zone grew rapidly, driven by the residual stress arising from fast cooling following LBW, whereas the unrecrystallized grains in base metal reminded relatively stable. The grain boundary lines in the T6 samples after the same etching procedure now appeared to be much finer as compared with the as-welded specimens, suggesting the decreasing extent of solute segregation near this regime and the back resolution of the grain boundary precipitates. In comparing the grains in Fig. 6(a) and (b) for the Ar and $N_2$ specimens, it was found that the grain size in the $N_2$ sample under the T6 condition was still smaller. This was partly because of the initial smaller grain size in the as-welded condition and partly because of the dispersed nitride particles inside the fusion zone which could slightly suppress grain growth.

## 3.5. Pore morphology and distribution

Close examination on the inner surfaces of the smaller pores in the Ar specimens consistently revealed the clear image of dendrite tips (Fig. 7(a)). There were a few instances that dendrite tips were not seen on the inner surfaces of the large pores, and in those cases oxides were formed on these local positions. The situation was different for the $N_2$ specimens. Dendrite tips in large pores were completely covered by multiple-coloured flake-like polygons (Fig. 7(b)), most likely nitrides. Even for small pores, the dendrite tips were not as apparent as those in the Ar specimens.

Systematic measurements of the porosity area fraction from the flat surfaces sectioned successively along the horizontal direction (i.e. on the longitudinal plane in Fig. 1, termed as $P_l$) or along the vertical direction (i.e. on the rolling plane, termed as $P_r$) have been done and the data on the highest area fraction along that direction ($P_{l,max}$ and $P_{r,max}$) are included in Tables III and IV for the Ar and $N_2$ cases. Examples of the typical spatial porosity distributions are presented in Fig. 8. The maximum porosity area fraction along the horizontal direction tended to occur at the centre of the fusion zone (Fig. 8(a)), except for specimens welded at low power and low speed where the distribution was either more random or characterized with two peaks near the fusion lines (Fig. 8(b)). The large pores located at the centre, which might be a result of the collapsed key-hole (as discussed in Section 4.2), were found to be the main contribution for the high porosity area fraction at the center. Fig. 8(c) gives the typical spatial distribution along the vertical direction for the unpenetrated specimens. In addition, the porosity area fraction was normally higher for the condition of "focus + 2" as compared with other focussing situations, suggesting that a higher heat absorption efficiency had occurred under this condition which would result in a high pore amount.

It was also noted that the pore shape was not always sphere-like, as the situation seen in EBW. For the Ar specimens, the pores in the fully penetrated samples viewed from both the rolling and longitudinal

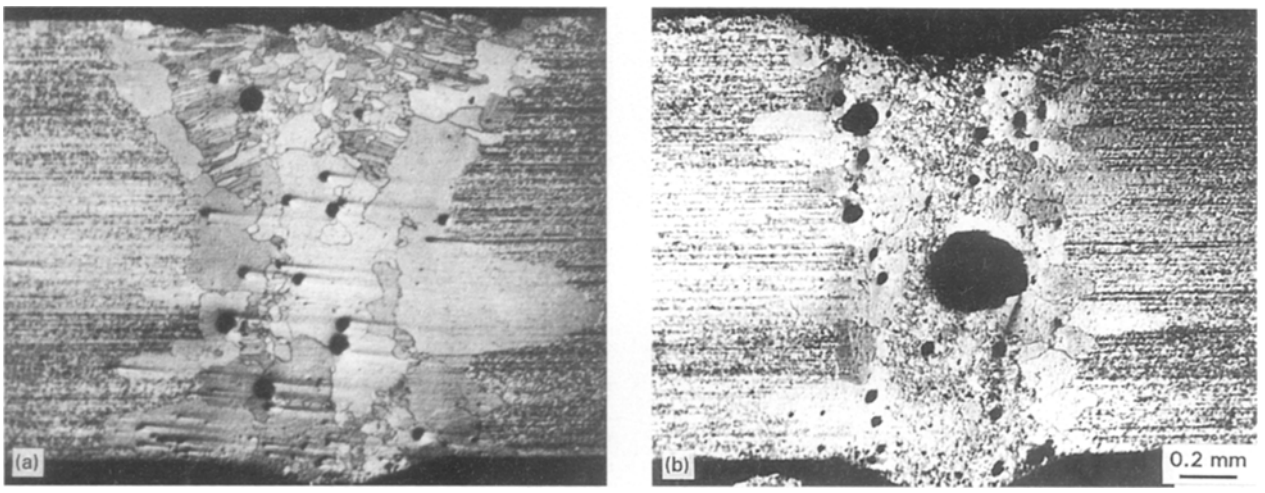


*Figure 6* Typical optical micrographs of the grain structure after a post-weld T6 treatment seen from the transverse plane of (a) the Ar specimen 516 and (b) the $N_2$ specimen 610.

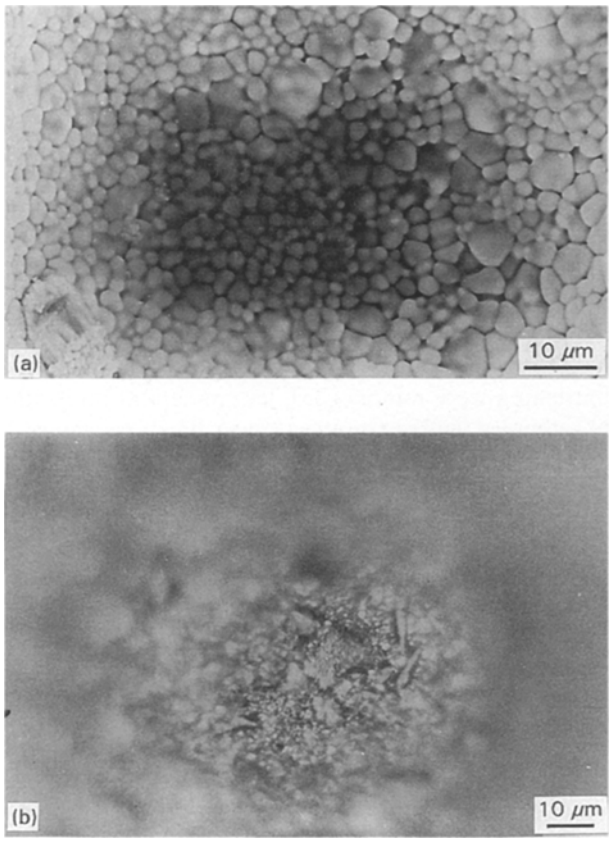


*Figure 7* (a) SEM micrograph showing the dendrite tips on the inner surface of a large pore in the Ar specimen 503, and (b) optical micrograph showing the flake- or sand-like layer on the inner surface of a large pore in the $N_2$ specimen 604.

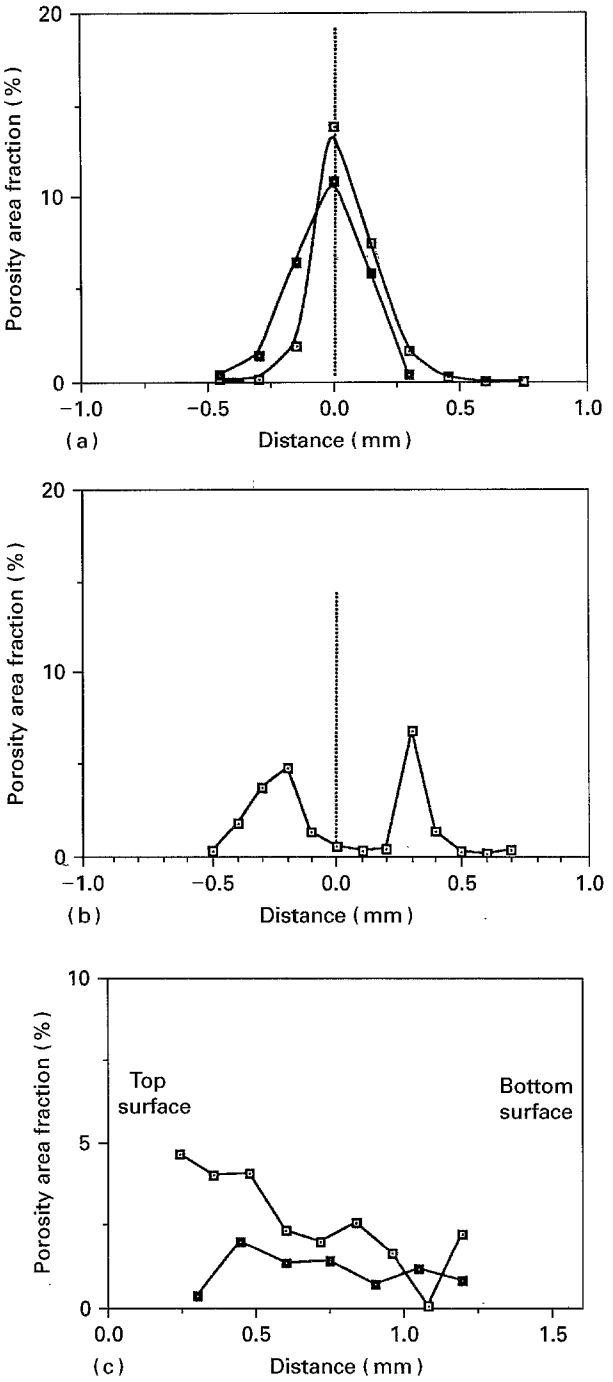


*Figure 8* Illustration of the spatial distribution of porosity area fraction measured from successive longitudinal planes ($P_l$) along the horizontal direction: (a) the typical distribution seen in most specimens, e.g. the Ar specimen 519 (□) and the $N_2$ specimen 614 (■), and (b) the distribution seen in samples welded at low power and low speed, e.g. the Ar specimen 501. The typical distribution measured from the successive rolling planes ($P_r$) along the vertical direction in the Ar specimen 519 (□) and the $N_2$ specimen 614 (■) is shown in (c).

planes (Fig. 9(a)) all exhibited a near spherical shape, and the area fractions of the porosity measured from rolling planes ($P_r$) as well as longitudinal planes ($P_l$) were compatible. In contrast, the pore shape in the unpenetrated samples was still spherical when viewed from the rolling plane but highly elongated when viewed from the longitudinal plane (the latter is shown in Fig. 9(b)). The $P_l$ readings were consistently higher than the $P_r$ data (Table III); this effect will be discussed in Section 4.3. The situation in $N_2$ specimens was similar, but the nearly spherical pores were more irregularly shaped and the elongated pores were more stretched along the long axis (Fig. 9(c)), both implying the faster cooling which had more effectively frozen the agitating melt flow.

In comparison with the porosity area fraction in the Ar and $N_2$ specimens, it can be seen that the former possessed higher but more scattered data than the latter ones under the same weld parameters. The average value of the maximum area fraction seen on the longitudinal and rolling planes was $P_{l,max} = 8.8 \pm 4.4\%$ and $P_{r,max} = 5.7 \pm 2.3\%$, respectively, for the Ar specimens, and was $P_{l,max} = 4.9 \pm 2.7\%$ and $P_{r,max} = 3.2 \pm 1.0\%$ for the $N_2$ samples. Further discussion will be covered in Section 4.1.

## 3.6. EPMA compositional analysis

The EPMA results of the LBWed specimens compared well with those obtained from the EBWed samples [6]. Mg loss inside the fusion zone was evident; Li cannot be detected but was thought to behave similarly to Mg. As for the samples welded using $N_2$, considerable N was detected on the inner surface of the large voids; whereas no apparent N was found near small pores. This suggested that the inner surfaces of large voids must have absorbed $N_2$ and formed nitrides during welding and such large holes might be filled with $N_2$ gases. The inner surfaces might be the original key-hole surfaces which were partially closed

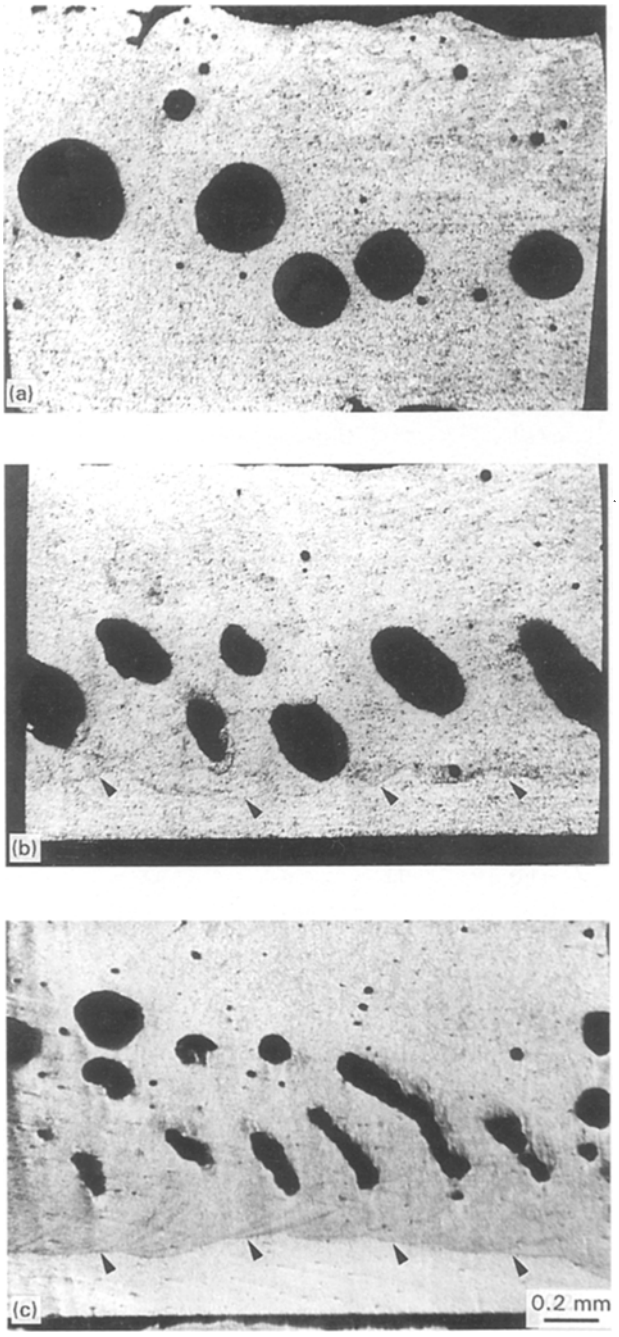


*Figure 9* Optical micrographs showing the pore morphology seen from the longitudinal plane of (a) the fully penetrated Ar specimen 507, (b) the unpenetrated Ar specimen 503, and (c) the unpenetrated $N_2$ specimen 611. The bottom fusion line is indicated by arrows in (b) and (c).

at the final stage so as to form individual large voids. These surfaces had extensively reacted with $N_2$ during welding. In contrast, the small pores, without the detection of N, should be originated from the interior by the evaporation of $H_2$, Li or Mg. Based on the current findings, the large and small pores seen in LBW specimens, for both the Ar and $N_2$ ones, might be formed by two different mechanisms.

## 3.7. Microhardness

The microhardness profiles of the LBWed specimens were similar to those of the EBWed samples [6]. The hardness was higher inside the fusion zone ($H_V \sim 73$–$83$), especially for the fusion line (85–90), than in base matrix (65–70), owing to the precipitation of δ′, S, $T_1$ and $T_2$ phases within the fusion zone during cooling. The microhardness readings inside the fusion zone were slightly higher in the Ar case ($H_V \sim 77$–$83$) than that in the $N_2$ case (73–77). This was consistent with the OM examination where it was found that the cooling rate must have been higher under $N_2$ so that smaller grain sizes and less precipitation resulted. Since the primary strengthening effect in Al–Li base alloys was contributed by precipitation hardening (contributions from solution and grain size hardening were minor) [26], less precipitation in the $N_2$ samples tended to reflect lower hardness values.

Upon undergoing the T6 temper, the hardness readings inside the fusion zone increased up to $\sim 140\ H_V$ for the Ar specimens and $\sim 145\ H_V$ for the $N_2$ ones, compared to the $\sim 150\ H_V$ in the BM. The relatively lower hardness in the fusion zone than that in the base metal was due to the loss of Li and Mg, as well as the much coarser grain size and incomplete back resolution of large precipitates leading to a lower volume fraction of strengthening δ′ precipitates [6]. The slightly higher reading in the T6 samples for the $N_2$ case were thought to be caused primarily by the less evaporation of Li and Mg during the faster cooling. Meanwhile, the fewer and smaller bulk $T_2$ precipitates in the AW samples welded under $N_2$ also helped to result in more complete back resolution during the T6 treatment, and thus a higher amount of strengthening δ′ precipitates and a higher value of microhardness.

## 3.8. Tensile tests

The tensile property of the as-received base metal was first evaluated. The average data on the engineering ultimate tensile stress (UTS) and elongation based on four separate tests were $270 \pm 9$ MPa and $11.6 \pm 1.1\%$, respectively. As for the base metal + T6 sample, the values were $424 \pm 9$ MPa and $6.1 \pm 0.7\%$.

For the as-welded and T6 specimens, it needs to be noted again that the surface unevenness and undercut, as well as the bottom unpenetrated part for those specimens that were not fully penetrated, were removed before testing. The UTS values of the as-welded specimens welded using Ar varied within 198–279 MPa with an average of $235 \pm 14$ MPa, as summarized in Table V. The average joint efficiency, defined by $UTS_{AW}/UTS_{BM}$, was around 87%. A similar level of UTS was seen for the $N_2$ cases, ranging from 198 to 254 MPa (Table VI), with an average of $238 \pm 12$ MPa and a joint efficiency of 88%. Both UTS results closely resembled those welded by electron beam under vacuum ($230 \pm 13$MPa) [6]. However, the average tensile strain of the as-welded samples using Ar or $N_2$ was $6.7 \pm 2.5\%$ or $5.3 \pm 1.3\%$, respectively, both considerably lower than the $9.9 \pm 1.7\%$ obtained from the EBW experiment [6] and the $11.6 \pm 1.1\%$ for the as-received base metal. This might be due to the larger pore size, irregular shape of the pores, and a higher content of impurities

TABLE V Summary of the post-weld tensile properties obtained from the Ar specimens

| No. | As-welded specimens | | T6 specimens | |
|---|---|---|---|---|
| | UTS (MPa) | Strain (%) | UTS (MPa) | Strain (%) |
| 501 | 234.2 ± 0.2 (86.7%)[a] | 10.2 ± 0.9 | 345.3 ± 5.4 (81.4%)[a] | 3.9 ± 0.3 |
| 502 | 234.3 ± 1.1 (86.7%) | 9.8 ± 1.1 | 354.2 ± 6.9 (83.5%) | 3.3 ± 0.0 |
| 503 | 236.7 ± 0.1 (87.4%) | 9.0 ± 0.7 | 324.1 ± 9.5 (76.4%) | 2.4 ± 0.2 |
| 504 | 244.9 ± 1.6 (90.7%) | 10.1 ± 0.3 | 352.4 ± 4.4 (83.1%) | 3.0 ± 1.0 |
| 505 | 277.3 ± 1.8 (102.0%) | 6.0 ± 0.4 | 370.6 ± 3.9 (87.4%) | 4.2 ± 0.1 |
| 506 | 238.4 ± 0.1 (88.3%) | 10.2 ± 0.8 | 329.5 ± 18.3 (77.8%) | 3.7 ± 0.3 |
| 507 | 235.2 ± 1.6 (88.2%) | 10.4 ± 1.6 | 336.2 ± 5.1 (79.3%) | 2.9 ± 0.3 |
| 508 | 235.4 ± 0.7 (87.2%) | 6.0 ± 0.7 | 326.3 ± 8.3 (76.9%) | 2.7 ± 0.3 |
| 509 | 238.0 ± 0.8 (88.1%) | 5.3 ± 0.4 | 354.7 ± 15.6 (83.6%) | 4.0 ± 0.9 |
| 510 | 234.4 ± 0.6 (86.8%) | 4.5 ± 0.3 | 369.6 ± 1.0 (87.2%) | 4.1 ± 0.1 |
| 511 | 237.4 ± 0.7 (87.9%) | 7.1 ± 0.2 | 317.2 ± 2.9 (74.8%) | 3.8 ± 0.4 |
| 512 | 205.9 ± 7.7 (76.2%) | 3.3 ± 1.2 | 319.7 ± 0.1 (75.4%) | 2.8 ± 0.1 |
| 513 | 211.9 ± 11.1 (78.5%) | 2.9 ± 0.5 | 352.0 ± 15.5 (83.0%) | 4.5 ± 1.1 |
| 514 | 249.1 ± 2.5 (92.2%) | 4.8 ± 0.2 | 355.2 ± 11.7 (83.8%) | 4.6 ± 0.6 |
| 515 | 233.5 ± 4.4 (86.5%) | 4.5 ± 0.5 | 351.7 ± 3.2 (82.9%) | 3.4 ± 0.6 |
| 516 | 235.3 ± 1.4 (87.1%) | 5.6 ± 0.3 | 331.7 ± 8.5 (78.2%) | 2.9 ± 0.1 |
| 517 | 227.3 ± 4.4 (84.1%) | 5.0 ± 0.7 | 334.1 ± 1.0 (78.9%) | 2.6 ± 0.2 |
| 518 | 226.8 ± 11.9 (84.0%) | 6.2 ± 0.3 | 341.5 ± 2.7 (80.5%) | 3.1 ± 0.0 |
| 519 | – | – | 361.3 ± 8.6 (85.0%) | 2.9 ± 0.4 |

[a] The values inside parentheses refer to the joint efficiency

TABLE VI Summary of the post-weld tensile properties obtained from the $N_2$ specimens

| No. | As-welded specimens | | T6 specimens | |
|---|---|---|---|---|
| | UTS (MPa) | Strain (%) | UTS (MPa) | Strain (%) |
| 601 | 234.9 ± 2.1 (87.0%)[a] | 6.5 ± 0.2 | 345.0 ± 6.5 (81.4%)[a] | 2.8 ± 0.3 |
| 602 | 241.6 ± 1.1 (89.5%) | 7.3 ± 0.1 | 346.1 ± 5.4 (81.6%) | 2.8 ± 0.1 |
| 603 | 242.1 ± 0.7 (89.6%) | 6.0 ± 0.2 | 332.2 ± 6.7 (78.3%) | 1.7 ± 0.3 |
| 604 | 244.9 ± 1.2 (90.7%) | 6.4 ± 0.3 | 341.3 ± 7.3 (80.5%) | 2.5 ± 0.2 |
| 605 | 247.4 ± 0.4 (91.6%) | 6.9 ± 0.3 | 339.2 ± 8.2 (80.0%) | 2.1 ± 0.2 |
| 606 | 245.4 ± 4.0 (90.9%) | 6.0 ± 0.0 | 339.3 ± 4.5 (80.0%) | 2.0 ± 0.4 |
| 607 | 245.8 ± 3.8 (91.0%) | 6.5 ± 0.4 | 357.3 ± 2.3 (84.2%) | 2.6 ± 0.1 |
| 608 | 238.5 ± 0.4 (88.0%) | 5.7 ± 0.1 | 333.8 ± 5.9 (78.7%) | 2.6 ± 0.3 |
| 609 | 240.2 ± 0.5 (88.9%) | 4.8 ± 0.2 | 342.2 ± 8.0 (80.7%) | 2.1 ± 0.1 |
| 610 | 220.8 ± 0.8 (81.8%) | 2.9 ± 0.2 | 329.1 ± 1.2 (77.6%) | 2.0 ± 0.3 |
| 611 | 232.0 ± 2.7 (85.9%) | 4.5 ± 0.1 | 340.8 ± 6.9 (80.4%) | 2.0 ± 0.3 |
| 612 | 220.9 ± 0.9 (81.8%) | 3.3 ± 0.2 | 337.1 ± 15.8 (79.5%) | 2.4 ± 0.5 |
| 613 | 231.0 ± 3.8 (85.6%) | 4.3 ± 0.4 | 332.4 ± 1.0 (78.4%) | 2.9 ± 0.3 |
| 614 | 203.2 ± 5.2 (75.2%) | 3.2 ± 0.6 | 323.9 ± 13.8 (76.4%) | 2.2 ± 0.4 |
| 615 | 248.4 ± 6.0 (92.0%) | 5.5 ± 0.2 | 351.2 ± 15.9 (82.8%) | 2.7 ± 0.2 |
| 616 | 243.6 ± 3.3 (90.2%) | 5.5 ± 0.6 | 339.4 ± 10.7 (80.0%) | 1.9 ± 0.4 |

[a] The values inside parentheses refer to the joint efficiency.

in samples welded by laser beam, particularly for the case when using $N_2$ gas.

After the T6 heat treatment, the Ar samples showed an average value of UTS of 343 ± 16 MPa and strain of 3.4 ± 0.7%, or an average joint efficiency of 81%. Those welded under $N_2$ exhibited UTS of 339 ± 8 MPa and strain of 2.3 ± 0.4%, or a joint efficiency of 80%. Both data are tabulated in Tables V and VI. These data indicated comparable UTS values in comparing with the EBW results (349 ± 22 MPa) but again appreciably lower strain values than those obtained using EBW (4.7 ± 0.6%). The post-weld tensile strengths for both the LBW or EBW specimens might be sufficient (above 80% of the base metal), but the tensile strain was lower than expected.

## 3.9. SEM fractography

The fractography of the tensile tested as-welded specimens LBWed under either Ar or $N_2$ showed ductile morphology with apparent dimples, similar to the case of EBW [6]. The main difference was the unusual large particles over 10 μm in size occasionally present in samples welded by laser beam, as shown in Fig. 10. These particles were identified by EPMA to be oxides for the samples welded using Ar and were mostly nitrides for the ones welded under $N_2$, both causing lower post-weld tensile strains as compared with the case of EBW. In the as-welded + T6 specimens, the fractography was characterized with brittle intergranular shearing appearance.

It was noticed that the inner surface morphology of the exposed pores on fracture surfaces was different in the Ar and $N_2$ specimens. No apparent surface layer but traces of limited plastic deformation can be seen in the Ar samples for both large and small pores. In contrast, in the $N_2$ samples there were hard and brittle-like nitride surface layers present on the surfaces of large pores, but not the small pores. These nitride layers were evidenced sometimes with numerous microcracks (Fig. 11(a)) and sometimes with exfoliated pieces (Fig. 11(b)). Interestingly, this phenomenon was not observed for the small pores in the $N_2$ samples, consistent with the EPMA results and suggesting the different formation origins for the large and small pores.


*Figure 10* SEM micrograph of the typical large particles seen in the $N_2$ specimens.

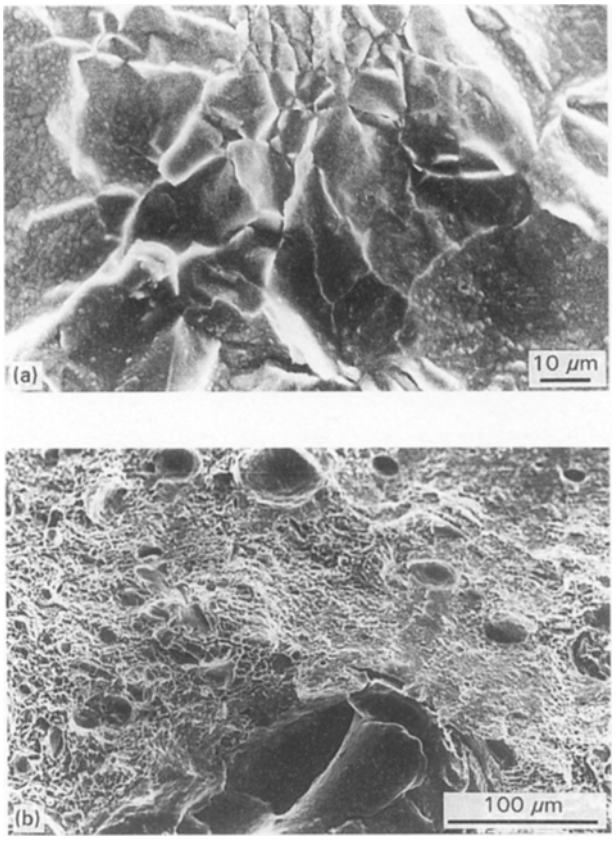


*Figure 11* SEM micrographs showing (a) the inner surface of a large pore and (b) the occasional occurrence of exfoliated nitride layers in the as-welded $N_2$ specimen after post-weld tensile test.

## 4. Discussion

### 4.1. Effects of using Ar or $N_2$ gas

#### *4.1.1. On the macro-appearances and microstructures*

It has been shown in Sections 3.1–3.4 that the width and cross-sectional area of the fusion zone in the $N_2$ samples were smaller than those in the Ar ones. This can be rationalized in terms of the different physical properties of the $N_2$ and Ar gases. Firstly, $N_2$ has higher thermal conductivity and heat capacitance and lower viscosity compared with Ar [27], all leading to a higher loss of laser-beam heat input and hence a lower fusion zone cross-sectional area. Secondly, the first layer ionization energy of the $N_2$ gas is lower than Ar, resulting in a severer plasma screening effect and thereby a lower heat input and also a lower cross-sectional area. However, generally in cases where plasma shadowing is severer, the fusion zone tends to become wider but shallower, contrary to the current situation for the $N_2$ specimens where the fusion zone became much narrower. Therefore, a third factor was thought to play a more important role, namely, the change of surface tension of the aluminium melt during LBW under different atmospheres. It has been shown that the surface tension of liquid aluminium under $N_2$ will be greater [29]. We postulated that this was probably due to the formation of nitride products on the liquid surface which will damage surface tension. The lower surface tension would favour the melt to flow inward and downward, and indirectly promoted key-hole formation and a highly narrow fusion zone.

Also due to the higher thermal conductivity of the $N_2$ gas, coupled with the smaller fusion zone cross-sectional area, the cooling rate for the specimens welded under $N_2$ was much higher than those under Ar. This can be justified by the much smaller grain size, limited precipitation, and the lower microhardness in the fusion zone of the as-welded $N_2$ specimens. It should be noted that such differences cannot be completely changed after a T6 treatment.

#### *4.1.2. On the post-weld mechanical properties*

For comparison, the data on the post-weld tensile stress and strain are plotted in Fig. 12 as a function of heat input for both the Ar and $N_2$ specimens. Contrary to the previous EBW results obtained under vacuum [6] where a clear decreasing trend was seen, the ultimate tensile stress showed a nearly constant behaviour over the entire heat-input range while the failure strain of the as-welded and T6 samples exhibited an increasing or slightly decreasing trend. Such an irregular result was not surprising since the values of heat input from the laser gun cannot reflect the actual heat absorbed. The complicated beam absorption and scattering effect associated with the induced plasma plume made the heat input value not any more a parameter which can be used as a direct indication for post-weld properties.

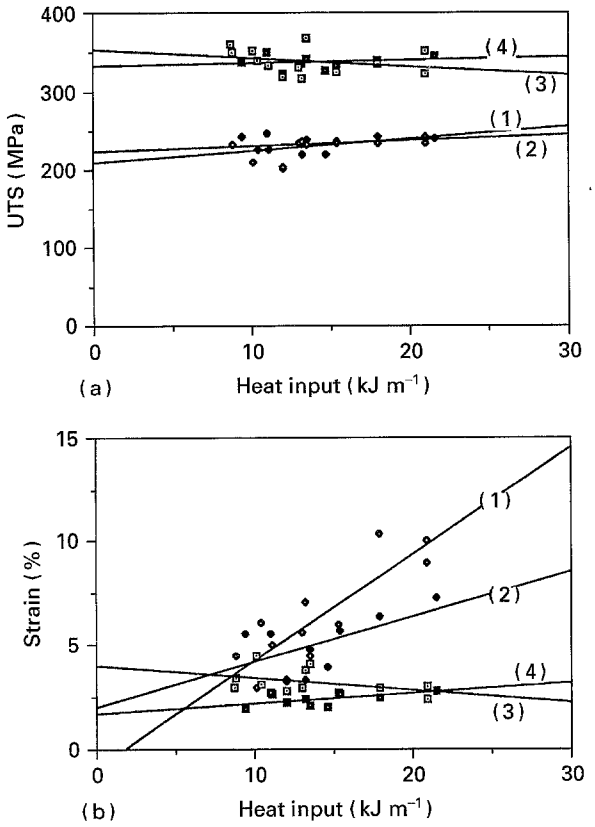


*Figure 12* The dependence of (a) post-weld ultimate tensile stress, and (b) tensile failure strain as a function of heat input for the Ar and $N_2$ specimens under the as-welded and T6 conditions. (a) ◇ (1) UTS-AW-Ar; ◆ (2) UTS-AW-$N_2$; ◘ (3) UTS-T6-Ar; ■ (4) UTS-T6-$N_2$; (b) ◇ (1) e-AW-Ar; ◆ (2) e-AW-$N_2$; ◘ (3) e-T6-Ar; ■ (4) e-T6-$N_2$.

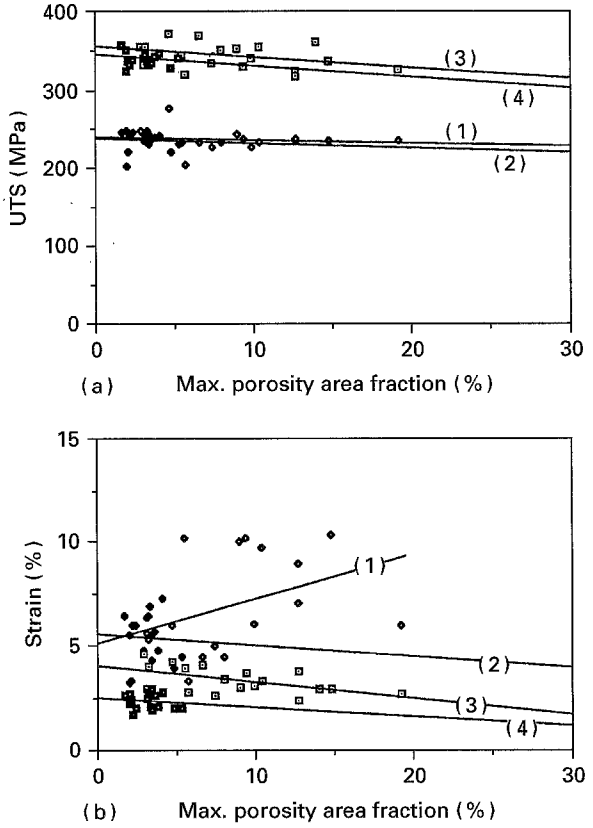


*Figure 13* The dependence of (a) post-weld ultimate tensile stress, and (b) tensile failure strain as a function of the maximal porosity area fraction measured from the longitudinal planes ($P_{l,max}$) for the Ar and $N_2$ specimens under the AW and T6 conditions. See Fig. 12 for key.

On the other hand, one might expect a close relationship imposed between the post-weld tensile properties and the porosity area fraction measured on the longitudinal plane since the tensile loading axis was perpendicular to this plane. Fig. 13 shows the plots of UTS and strain data as a function of the maximum porosity area fraction ($P_{l,max}$). Basically, the tensile stress and strain data in Fig. 13 for both the Ar and $N_2$ specimens under the as-welded or T6 condition, though subjected to large scattering, were seen to show a slightly decreasing trend with increasing porosity amounts. One exception was the strain data obtained from the as-welded Ar specimens. In this case the scattering was much larger than others, making the line fitting highly questionable. It must be reminded that the data on pore area fraction were affected by another factor related to the geometrical difference of the pore (spherical or elongated), making the dependency in Fig. 13 less apparent. This issue will be discussed in Section 4.3. Disregarding this factor, it appeared that the spherical or elongated pores did not induce high stress-concentration and would not affect the post-weld tensile properties as severely as one might expect.

Since the difference in the average post-weld UTS values obtained from the Ar and $N_2$ specimens in both the AW and T6 conditions was no more than 2%, it may be safely stated that the use of cheaper $N_2$ gas will not really degrade the post-weld failure strength. Nevertheless, we did observe some differences in the yield stress of the Ar and $N_2$ samples which were related to the small differences in precipitation behavior and were in turn related to the differences in cooling rate under Ar or $N_2$ atmosphere. On the other hand, a significant decrease in post-weld tensile strain by 25–50% was seen when using $N_2$. Such a serious drop of elongation cannot be avoided since nitride particles will always form. The application of $N_2$ gas in welding aluminium alloys containing active elements such as Li and Mg may be unacceptable, judging from the low post-weld elongation.

## 4.2. Porosity formed during LBW

The porosity formed in the current alloy during welding may be caused by (1) the hydrogen-enriched surface layer; (2) Li and/or Mg vapour (both Li and Mg have very high vapour pressure); (3) the absorption of gas or impurities from atmosphere or fillers during welding; and (4) the voids formed directly through the collapsed key-hole which is filled with the blowing gas such as Ar or $N_2$.

The previous study [6] has demonstrated the major and minor contributions from the hydride and Li/Mg evaporation, respectively, in forming porosity in superplastic-grade 8090 alloys when EBWed under vacuum. The pore spatial distribution in the EBWed specimens was basically random [6]. However, in the present experiment more pores and a larger size of

pores were consistently observed near the central line of the fusion zone when welded by laser beam under either Ar or $N_2$. Similar observations have also been reported by Whitaker *et al.* [19]. Since the inner surface of the retained large pores near the central line contained apparent nitride layers in the $N_2$ specimens, but not for the small and randomly-distributed pores, it was likely that those large pores dispersed near the centre were a result of collapsed key-holes during solidification. This would most likely occur when the key-hole was continuously blown with Ar or $N_2$ gas from the top, as in the case of LBW but not for EBW under vacuum. However, for those specimens welded at low power and low welding speed (e.g. the 501 sample in Fig. 8(b)), no deep key-hole was formed and thus the pore distribution was completely reversed. The local higher pore area fraction at two sides in Fig. 8(b) was due to a higher cooling rate near the fusion line, thus freezing the voids due to $H_2$ or Li/Mg evaporation before they could escape to the top surface.

## 4.3. Pore shape and pore area fraction

Since the large pores were most likely formed from key-holes, the pore shape was also affected by this mechanism. From Section 3.5. it can be seen that the pore shape seen from the top or side section of the weld line was all sphere-like in the fully penetrated specimens but highly elongated when viewed from the longitudinal plane of the unpenetrated samples. This was because when the fusion zone was not fully penetrated, the lower portion of the key-hole during welding would tend to be stretched backward, instead of being vertical. Upon rapid cooling, the large pores formed from the collapsed key-hole would retain a stretched and elongated shape, with a long axis $\sim 45°$ with respect to the welding directions when seen from the longitudinal plane. As the weld became penetrated, the vapour pressure could be released from the bottom surface and a different pressure balance was established. The pores formed in this case tended to be spherical. Fig. 14 is an example showing the change of pore shape from the unpenetrated to penetrated region.

It has been stated in Section 3.5 that $P_{l,max}$ and $P_{r,max}$ for penetrated specimens were compatible, whereas in the unpenetrated samples the $P_{l,max}$ values were much higher than the $P_{r,max}$ readings. This was actually caused by the geometry. For two pores of identical volume, one is a sphere (with a radius $r$ and a planar radius $r_s$ where $r_s = kr$ and $k \sim 0.78$) and the other is of elongated peanut-like shape (with long axis $L = nr_s$ where $n$ can vary between 1 and 5 for the current case) inclined $\sim 45°$ with respect to the sheet surface, it can be easily proved that the ratio of these two cross-sectional areas seen from the longitudinal section is

$$\text{Ratio} = (\pi + 2n)/\{\pi[(4 + 3nk)/4]^{2/3}\}$$

The higher the $n$ value or the more elongated the pore is, the higher ratio will be. Thus for a typical pore shape with $n \sim 2.5$, a factor of 1.4 difference will be

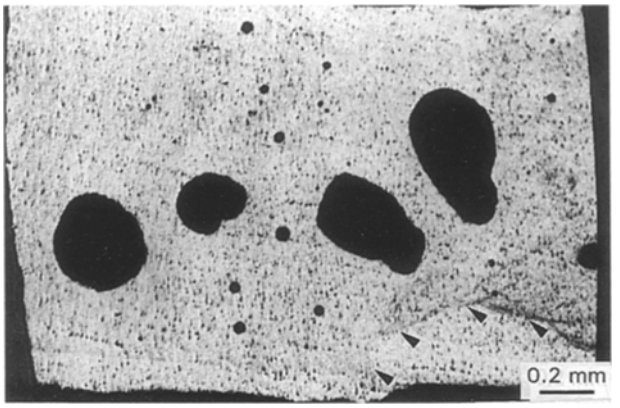


*Figure 14* SEM micrograph illustrating the shape change of the pores from elongated shape in the unpenetrated part to nearly spherical phase in the fully penetrated part. The bottom fusion line is indicated by arrows.

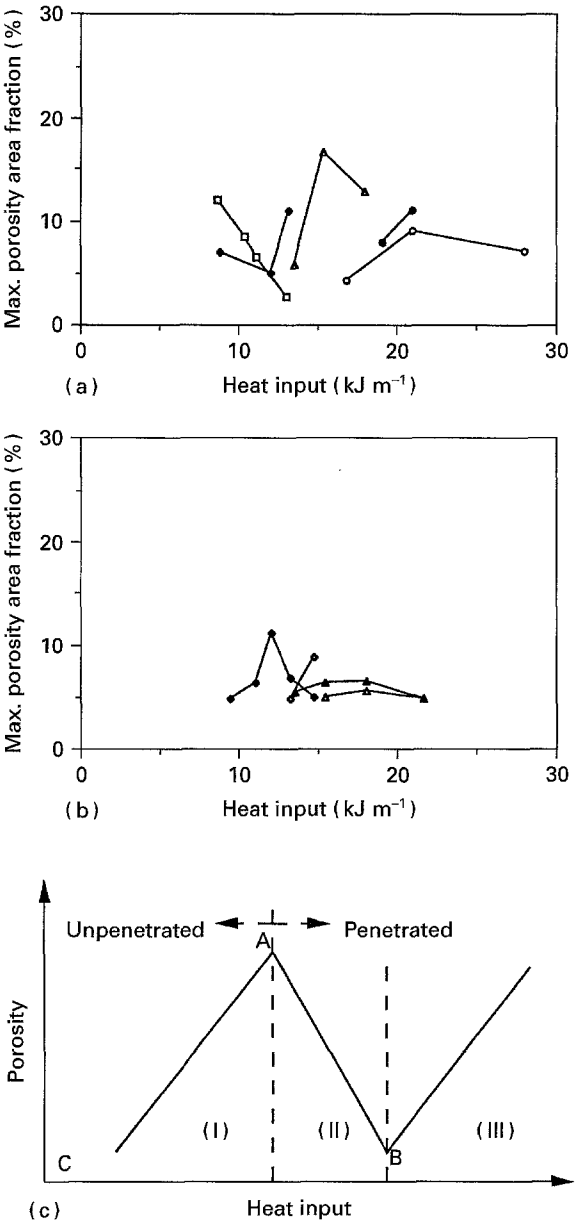


*Figure 15* Showing the dependence of the maximum porosity area fraction. ($P_{l,max}$) as a function of heat input for (a) the Ar and (b) the $N_2$ specimens. The postulated relationship is presented in (c) where in regions (I) and (III) a regular increasing trend is followed and in region (II) an abnormal decrease is observed as a result of the pore shape change. See Fig. 3 for key.

obtained if we measure the pore cross-sectional area from the side view and top view, respectively. This was the main reason for the different readings of $P_{l,max}$ and $P_{r,max}$ measured from the unpenetrated specimens.

Fig. 15 gives the dependence of pore area fraction ($P_{l,max}$) for the same focusing condition versus heat input. By close examinations, it was noticed that there existed a discontinuous jerk whenever the weld changed from near penetration to full penetration, or the pore changed from elongated to spherical shape when viewed from the longitudinal section. The geometrical factor has partly made the readings of $P_{l,max}$ also not a simple function of heat input. A drawing shown in Fig. 15(c) is our simplified illustration of the current situation. Region I and III in Fig. 15(c) represent the normal trend where the pore area fraction increases with increasing heat input, and Region II is the abnormal drop due to shape change. The overall trend between $P_{l,max}$ and heat input was thus less apparent. By using the data on $P_{l,max}$ to relate to the post-weld mechanical properties, as shown in Section 4.1.2, it was inevitable that the trend was not highly apparent.

## 4.4. Comparison between LBW and EBW

The comparisons of the weld parameters used and the associated characteristics between LBW under Ar and $N_2$ atmospheres and EBW under vacuum are presented in Table VII. LBW seemed to require a much higher beam power and heat input for compatible weld depths. Meanwhile, for similar levels of weld depth, the fusion zone width in LBWed samples was much smaller, especially for the $N_2$ specimens.

Since the cooling rate during LBW was much faster due to mainly gas blowing, the solidified FZ retained more of the melt agitation, also resulting in a more uneven surface, less hot cracking tendency, and finer grain structures. The occasional occurrence of hot cracking during EBW with high heat input was never observed in LBW. The higher cooling rate during LBW reduced the tendency of severe solute segregation and coarse precipitation along grain boundaries, and in turn suppressed the hot cracking along grain boundaries as seen during EBW [6].

The primary difference between LBW and EBW might be the porosity amount and their major formation mechanism. Hydrogen evaporation during EBW under vacuum was considered to be the main cause for pore formation, while the incomplete closure of Ar- or $N_2$-filled key-holes during rapid solidification was the key contributor for the high porosity volume fraction. The latter in turn lead to the lower post-weld tensile elongation for the LBWed specimens.

## 5. Conclusions

On the basis of the current results on LBW performed on an uncrystallized 8090 thin sheet, the following conclusions may be drawn:

1. Although subjected to a high reflectivity during the initial stage, the current alloy can still be satisfactorily LBWed. The higher the power and welding speed were, the more uneven the fusion zone surface and the more severe the undercut problem became. With increasing heat input, the fusion zone cross-sectional area and depth/width ratio basically showed an increasing trend, except for the high power cases where plasma-screening effect was severe.
2. By using a focusing condition 2 mm below the sheet top surface, the best heat absorption by the 1.6 mm-thick specimens was achieved. However, the "focus + 1" condition tended to produce lower porosity amounts, though leading to a more shallow fusion zone.
3. The post-weld tensile failure strengths for both the Ar and $N_2$ specimens, though possessing a considerable amount of pores, were still varied around 235 and 340 MPa under the as-welded and T6 condition, respectively, or equivalent to a joint efficiency approximately 80–90% of the base metal. However, the post-weld failure strain was of the order 5–7% for the as-welded samples and 2–3% for the T6 ones,

TABLE VII Comparison between the experimental parameters and weld characteristics of the laser-beam welding using Ar or $N_2$ and electron-beam welding under vacuum

| Item | LBW, using Ar | LBW, using $N_2$ | EBW, under vacuum |
|---|---|---|---|
| Power of beam (W) | 700–1300 | 900–1100 | 240–360 |
| Welding speed (mm min$^{-1}$) | 1500–9000 | 2500–7000 | 3000–4800 |
| Heat input (kJ m$^{-1}$) | 8.7–28.0 | 9.4–21.6 | 3.1–6.6 |
| Average $A_f$ (mm$^2$) | 1.16 ± 0.39 | 0.84 ± 0.29 | 1.48 ± 0.52 |
| Average $D$ (mm) | 1.38 ± 0.19 | 1.41 ± 0.15 | 1.39 ± 0.18 |
| Average $W$ (mm) | 1.40 ± 0.21 | 1.02 ± 0.07 | 1.61 ± 0.40 |
| Average $D/W$ | 1.00 ± 0.18 | 1.38 ± 0.11 | 0.81 ± 0.08 |
| Cooling rate | intermediate | fast | slow |
| Main origin of pores | collapsed key-holes | collapsed key-holes | hydrogen evaporation |
| Average $P_{l,max}$ (%) | 8.8 ± 4.4 | 4.9 ± 2.7 | ~ 2% |
| Mg and Li evaporation | low | low | high |
| Average $H_V$ inside FZ, AW | 80 ± 5 | 75 ± 5 | 78 ± 5 |
| Average $H_V$ inside FZ, T6 | 140 ± 5 | 145 ± 5 | 135 |
| UTS. as-welded (MPa) | 235 ± 14 | 238 ± 12 | 230 ± 13 |
| UTS, T6 (MPa) | 343 ± 16 | 339 ± 8 | 349 ± 22 |
| Strain, as-welded | 6.7 ± 2.5 | 5.3 ± 1.3 | 9.9 ± 1.17 |
| Strain, T6 (%) | 3.4 ± 0.7 | 2.3 ± 0.4 | 4.7 ± 0.6 |

considerably lower than the original ~10% (as-received) and 5% (as-received + T6) for the base metal. The presence of large nitride particles resulted in tensile elongation values in the $N_2$ specimens consistently smaller than those in the Ar specimens.

4. In comparison with the case using Ar gas, blowing $N_2$ gas was considered to reduce the melt surface tension, further promoting the inner and downward flowing tendency. This will directly result in a narrow deep fusion zone. Since $N_2$ has a higher thermal conductivity and heat capacitance and a lower viscosity relatively to Ar, the $N_2$ specimens were subjected to a higher loss of laser-beam heat input and a higher cooling rate, leading to a smaller fusion zone cross-sectional area, a finer grain size, limited precipitation, and a lower microhardness reading. The faster cooling rate can also help to freeze the elongated pore shape during rapid solidification when the weld was not fully penetrated.

5. The primary formation mechanism for large pores near the central line of LBWed specimens was thought to be a result of unescaped collapsed key-holes which have been filled with gases or plasma. This was contrary to the case of EBW processes where hydrogen bubbles were the key origin.

6. In comparison with the EBW results, LBW for 8090 alloys was characterized with a higher fusion-zone depth/width ratio, cooling rate, and porosity amount, and a lower solute loss and post-weld tensile strain.

## Acknowledgements

The authors wish to thank the Aero Industry Development Center of Taiwan for supplying the SPF-8090 sheets, and to Mr S. C. Chen and Mr J. S. Ku for technique support. The sponsorship from the National Science Council of Taiwan is gratefully acknowledged.

## References

1. R. GRIMES and R. G. BUTLER, in "Superplasticity in aerospace", edited by H. C. Heikkenen and T. R. McNelley (Warrendale, PA, TMS, 1988) p. 97.
2. P.-J. WINKLER, in "Superplasticity and superplastic forming", edited by C. H. Hamilton and N. E. Paton (Warrendale, PA, TMS, 1988) p. 491.
3. D. V. DUNFORD and P. G. PARTRIDGE, in Proceedings of the International Conference on Superplasticity in Advanced Materials (ICSAM-91), edited by S. Hori, M. Tokizane and N. Furushiro (Osaka, Japan, The Japan Society for Research on Superplasticity, 1991) p. 795.
4. D. V. DUNFORD, C. J. GILMORE, and P. G. PARTRIDGE, in Proceedings of the Sixth Aluminium–Lithium Conference, edited by M. Peters and P.-J. Winkler (Oberusel, Germany, DGM, 1992) p. 1057.
5. N. RIDLEY and D. W. LIVESEY, in Proceedings of the Sixth Aluminium–Lithium Conference, edited by M. Peters and P.-J. Winkler (Oberusel, Germany, DGM, 1992) p. 1063.
6. J. C. HUANG, Y. D. SHEN, and N. J. HO, *Mater. Sci. Tech.* **10** (1994) 647.
7. V. N. MIRONENKO, V. S. EVSTIFEEV and S. A. KURSHUNKKOVA, *Welding Production (USSR)* **26** (1979) 30 (in English).
8. D. M. BOWDEN and P. L. MESCHTER, *Scripta Metall.* **18** (1984) 963.
9. C. E. CROSS, D. L. OLSON, G. R. EDWARDS and J. F. CAPES, *Welding Res. Suppl.* **July** (1985) 241-s.
10. R. P. MARTUKANITZ, C. A. NATALIE and J. O. KNOEFEL, *J. Metals* **39** (1987) 38.
11. T. A. MARSICO and R. KOSSOWSKY, in Proceedings of the Fifth Aluminium–Lithium Conference, edited by T. H. Sanders and E. A. Starke (Birmingham, MCEP, 1989) p. 1447.
12. P. A. MOLIAN and T. S. SRIVATSAN, *J. Mater. Sci.* **25** (1990) 3347.
13. J. L. CANABY, F. BLAZY and J. F. FRIES, *Mater. Sci. Eng.* **A136** (1990) 131.
14. T. S. SRIVATSAN and T. S. SUDARSHAN, *Welding Res. Suppl.* **July** (1991) 173-s.
15. L. S. KRAMER and J. R. PICKENS, *Ibid.* **April** (1992) 115-s.
16. B. BIERMANN, R. DIERKEN, R. KUPFER, A. LANG and H. W. BERGMANN, in Proceedings of the Sixth Aluminium–Lithium Conference, edited by M. Peters and P.-J. Winkler (Oberusel, Germany, DGM, 1992) p. 1159.
17. E. YU, G. LI and Z. WANG, in Proceedings of the Sixth Aluminium–Lithium Conference, edited by M. Peters and P.-J. Winkler (Oberusel, Germany, DGM, 1992) p. 1191.
18. A. RAVINDRA, E. S. DWARAKADASA, T. S. SRIVATSAN, C. RAMANATH and K. V. V. IYENGAR, *J. Mater. Sci.* **28** (1993) 3173.
19. I. R. WHITAKER, D. G. McCARTNEY, N. CALDER and W. M. STEEN, *Ibid.* **28** (1993) 5469.
20. A. RAVINDRA, A. BANDYOPADHYAY, E. S. DWARAKADASA and T. S. SRIVATSAN, *Ibid.* **29** (1994) 1203.
21. M. G. CHOU, G. H. LIU, U. C. CHUANG, W. L. LAY and C. W. YANG, " Laser processing technique handbook" (Tsingchu, Taiwan, ITRI, 1989) p. 2–14 (in Chinese).
22. H. U. FRITSCH, in "Laser treatment of materials", edited by B. L. Mordike (Oberusel, Germany, DGM, 1987) p. 19.
23. T. R. ANTHONY and H. E. CLINE, *J. Appl. Phys.* **48** (1977) 3888.
24. K. C. MILLS and B. J. KEENE, *Int. Mater. Rev.* **35** (1990) 185.
25. T.-R. CHEN and J. C. HUANG, *Chinese J. Mater. Sci.* **25** (1993) 34.
26. J. C. HUANG and A. J. ARDELL, *Acta Metall.* **36** (1988) 2995.
27. R. C. WEST (ed), "CRC Handbook of Chemistry and Physics, 66th edition" (CRC Press, Boca Raton, FL, 1985–1986) p. E-2; D-178; F-42 and F-44.
28. A. PAUL and T. DEBROY, *Metall. Trans.* **19B** (1988) 851.

*Received 1 December 1994*
*and accepted 8 September 1995*